A circumbinary debris disk
in a polluted white dwarf system

J. Farihi[1,5*], S. G. Parsons[2,3], B. T. Gänsicke[4]

[1]Department of Physics and Astronomy, University College London, London WC1E 6BT, UK
[2]Departamento de Física y Astronomía, Universidad de Valparaíso, Valparaíso 2360102, Chile
[3]Department of Physics and Astronomy, University of Sheffield, Sheffield S3 7RH, UK
[4]Department of Physics, University of Warwick, Coventry CV5 7AL, UK
[5]STFC Ernest Rutherford Fellow

[*]To whom correspondence should be addressed; E-mail: j.farihi@ucl.ac.uk

Planetary systems commonly survive the evolution of single stars, as evidenced by terrestrial-like planetesimal debris observed orbiting and polluting the surfaces of white dwarfs (*1, 2*). This letter reports the identification of a circumbinary dust disk surrounding a white dwarf with a substellar companion in a 2.27 hr orbit. The system bears the dual hallmarks of atmospheric metal pollution and infrared excess (*3, 4*), however the standard (flat and opaque) disk configuration is dynamically precluded by the binary. Instead, the detected reservoir of debris must lie well beyond the Roche limit in an optically thin configuration, where erosion by stellar irradiation is relatively rapid. This finding demonstrates that rocky planetesimal formation is robust around close binaries, even those with low mass ratios.

The formation and evolution of planetary systems around close binary stars is a challenging problem, yet provides insight into the growth of planetesimals within evolving protoplanetary disks and planet formation in general. The small but increasing number of transiting circumbinary planets detected with *Kepler* (*5, 6*) are providing the first tests of theoretical formation models. To date, it has been shown that in situ formation is unfavorable for most of these Neptune- to Jupiter-sized bodies due to the destructive, dynamical effects of the central binary on planetesimal agglomeration in the regions where the planets currently orbit (*7–9*). However, for a range of masses including small planets, recent models predict favorable conditions for planetesimal growth within the snow line, and thus promoting efficient terrestrial planet formation around binaries (*10–12*).

Atmospheric pollution in white dwarf stars offers a unique and powerful window into the assembly and chemistry of terrestrial exoplanets. There are now more than three dozen planetary system remnants made evident based on thermal and line emission from circumstellar disks (*2*), and several hundred where photospheric metals indicate ongoing or recent accretion of planetary debris (*13*). The current paradigm of disrupted and accreted asteroids has been unequivocally confirmed by numerous studies, including the recent detection of complex and rapidly evolving photometric transits from debris fragments orbiting near the Roche limit of one star (*14–16*). To date, all polluted white dwarfs with detailed analyses indicate the sources are rocky planetesimals comparable in both mass and composition to large Solar System asteroids (*1, 17, 18*), and thus objects that formed within a snow line. These findings unambiguously demonstrate that large planetesimal formation in the terrestrial zone of stars is robust and common.

Until now, over 90% of such dusty and polluted white dwarf systems have been discovered among single stars, with a small fraction belonging to sufficiently wide binaries ($a \gg 100\,\mathrm{AU}$) where the evolution of each star – and any associated planetary system – proceeds as a singleton.

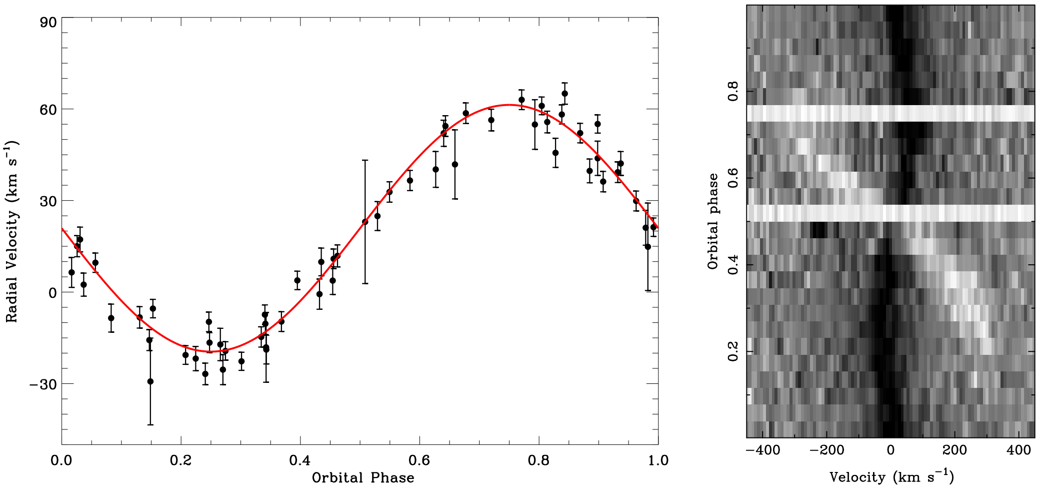

Figure 1: Phased radial velocity diagrams. The left panel plots the phased radial velocities for SDSS 1557 based on measurements of the Mg II absorption line and their associated errors (see Methods), with the resulting parameters given in Table 1. The right panel shows a trailed spectrum for the Hα component of SDSS 1557, where darker features represent lower fluxes and lighter features indicate higher fluxes. The absorption component follows identically that of Mg II, and thus both features are intrinsic to the white dwarf photosphere. The emission component is observed in anti-phase with the primary, and therefore originates from the irradiatively heated companion. The two horizontal blank lines represent phase bins without coverage.

The white dwarf SDSS J155720.77+091624.6 (hereafter SDSS 1557) exhibits strong infrared excess from $T \approx 1100$ K dust, and possesses one of the highest known metal abundances (*3, 4*), but has a distinctive low mass ($M \lesssim 0.45\, M_{\odot}$) that indicates a helium core. Such white dwarf masses are too low for single stars to attain within the age of the Galaxy, implying SDSS 1557 belongs to a class of remnants whose evolution was truncated prior to helium ignition (*19, 20*). These low-mass, helium core white dwarfs are often found to be short-period, spectroscopic binaries (*21*), consistent with efficient (common) envelope ejection during the first ascent giant branch.

SDSS 1557 was observed on multiple occasions with the GMOS and X-Shooter spectrographs at Gemini Observatory South and the Very Large Telescope respectively. The lower resolution GMOS data hinted at radial velocity changes in the Mg II 4482 Å absorption feature, and the higher resolution X-shooter data set reveal a robust period of 2.273 hr with semi-

White Dwarf Primary		Binary	
		p (h)	2.273153 ± 0.000002
SpT	DAZ	t_0 (HJD)	2457201.0551 ± 0.0004
g (AB mag)	18.43	K_1 (km s^{-1})	40.42 ± 0.69
$T_{\rm eff}$ (K)	$21\,800 \pm 800$	K_2 (km s^{-1})	288.3 ± 3.0
log g (cm s^{-2})	7.63 ± 0.11	γ_1 (km s^{-1})	20.91 ± 0.51
M_1 ($M_\odot$)	0.447 ± 0.043	γ_2 (km s^{-1})	6.2 ± 1.4
$\log(L/L_\odot)$	-1.25 ± 0.08	z (km s^{-1})	14.7 ± 1.5
Cooling Age (Myr)	33 ± 5	M_2 ($M_\odot$)	0.063 ± 0.002
d (pc)	520 ± 35	i (°)	62 ± 3
		a ($R_\odot$)	0.70 ± 0.02

Table 1: Stellar and binary parameters. White dwarf parameters $T_{\rm eff}$ and log g were derived from fitting atmospheric models to the higher Balmer lines for individual X-shooter spectra, and the adopted errors are the standard deviation from all 60 measurements. Errors in derived stellar parameters were calculated by propagating the uncertainties in the adopted $T_{\rm eff}$, log g, and published photometry through white dwarf evolutionary models (*19*). The binary and companion parameters, including errors, were calculated from analysis of the radial velocity measurements of the Mg II line in all X-shooter spectra (see Methods), and Kepler's laws. Note t_0 is defined as the inferior conjunction of the white dwarf, and K_2 is calculated assuming the observed emission is uniformly spread across the inner hemisphere of the companion.

amplitude $K_1 = 40.4\,\mathrm{km\,s^{-1}}$ (Figure 1). A close examination of the Hα region reveals an emission feature arising from the irradiated companion, seen in anti-phase and with semi-amplitude of 267.6 km s^{-1}. Assuming the emission is uniformly spread across the inner hemisphere of the companion, this implies a binary mass ratio $M_2/M_1 = 0.14$. Both the radial velocity data and the spectral energy distribution are consistent with a substellar companion of $0.063\,M_\odot$ (66 $M_{\rm Jup}$) seen at an orbital inclination near 63°. Table 1 lists all system parameters with uncertainties.

Figure 2 shows the expected infrared emission from a mid-L type substellar companion at the white dwarf distance based on the derived stellar parameters. Ultracool dwarfs earlier than L3 can be firmly ruled out, as the expected fluxes blueward of 2 μm would be significantly brighter than those observed. At the same time, the substellar companion cannot account for the total excess emission in the system over the $2 - 5\,\mu$m region, as the 4.5 μm flux is 5 to 6 times larger than expected for an L3 or L5 type dwarf (*22*). Even in the extreme case where

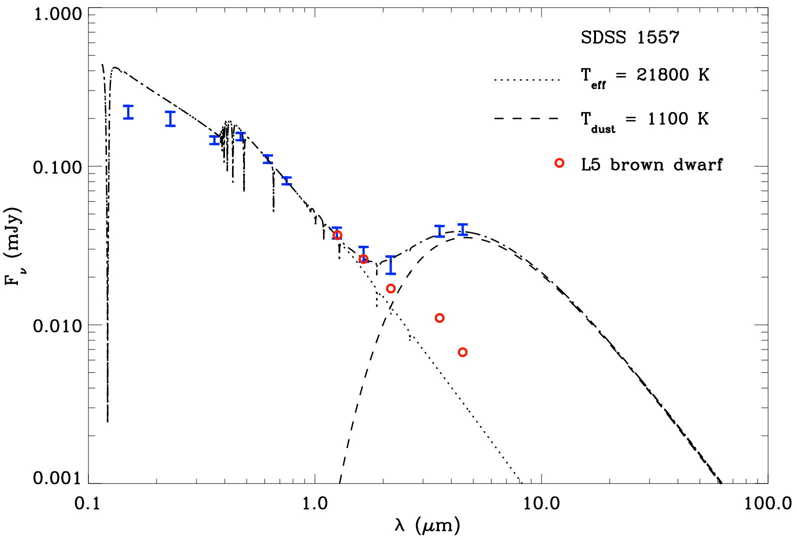

Figure 2: Spectral energy distribution. Previously reported multi-wavelength photometric data for SDSS 1557 are plotted as blue error bars (*4*), with the stellar flux from a pure hydrogen atmospheric model is shown as a dotted line. Overplotted as a dashed line is an 1100 K blackbody fitted to the strong, infrared dust emission, and an L5-type brown dwarf is shown as red circles; any companion earlier than L3 is ruled out by the photometry below 2 μm. The measured 4.5 μm flux from the system is between 5 and 6 times brighter than any allowed companion, and hence must be due to circumbinary dust. There is a notable deficit in ultraviolet flux relative to the stellar model, but a metal-rich atmosphere cannot account for the mismatch; neither the photospheric opacity nor the emergent flux are strongly affected by the presence of trace metals in a hydrogen-rich star of this temperature. The presence of a vertically extended dust shell may account for additional extinction at these shortest wavelengths.

the predicted 4.5 μm flux from a mid-L type companion is nearly doubled – mimicking the peak-to-peak changes seen in related systems due to irradiation from the primary (*23*) – the observed flux remains significantly higher. SDSS 1557 thus has both a strong infrared excess and atmospheric metal pollution at high abundance. It is therefore similar to more than three dozen known white dwarfs that are accreting planetary debris from circumstellar reservoirs that are consistent with tidally disrupted minor planets.

The identification of orbiting dust and atmospheric pollution within a close binary presents a fundamental challenge to the disk modeling, as the canonical flat and opaque ring geometry is dynamically prohibited. This standard disk would nominally be completely contained between 0.4 and 0.9 $R_\odot$ from SDSS 1557 (*4*). However, for a non-eccentric orbit, a companion of mass

$M_2 = 0.063\,M_\odot$, and a semimajor axis $a = 0.70\,R_\odot$, stable *circumstellar* orbits are allowed within $0.4a \approx 0.3\,R_\odot$ of the primary, and stable *circumbinary* orbits are allowed beyond $2.0a \approx 1.4\,R_\odot$ (*24*). The emitting dust cannot lie interior to $0.3\,R_\odot$, where even shielded grains would attain $T > 1700\,$K and thus be inconsistent with the observed thermal emission. Therefore the solid material must lie exterior to $1.4\,R_\odot$, but at this distance a flat, opaque disk would be no warmer than 500 K, and by itself inconsistent with the infrared data. Blackbody grains with $T = 1100\,$K will have an orbital radius of $3.3\,R_\odot$ in this system; this is the only configuration consistent with both the observed emission and the dynamical effects of the binary. Figure 3 provides an illustration of the system.

This $T_{\rm eff} = 21\,800\,$K hydrogen-rich white dwarf has a heavy element sinking timescale of only a few weeks (*25*), and observations of the Mg II feature include detections in 2010 April, 2012 May, 2014 May, and 2016 July, with no observed change in line strength. Thus SDSS 1557 is in a steady state of accretion from the circumbinary disk; the inferred accretion rate is $\dot{M} \simeq 6 \times 10^8\,{\rm g\,s^{-1}}$ assuming a bulk Earth abundance for Mg. Captured material from the companion – with solar abundance Mg – can be dismissed as the source of atmospheric enrichment, since this would require the brown dwarf to either 1) have a wind rate higher than the solar value (*26*), or 2) be twice its normal size to overfill its Roche lobe. It is noteworthy that the similar and even closer binary WD 0137–349 neither exhibits atmospheric metals nor an infrared excess above that expected for its components (*27*).

This is the first case of dusty debris inferred to be exterior to the Roche limit of a metal-accreting white dwarf (*28, 29*). The surrounding reservoir was likely created via binary driving of debris generated during a catastrophic fragmentation interior to the Roche limit. Material must flow onto the stellar surface via stable streaming from the inner edge of the circumbinary disk, where solids will gradually sublimate as they spiral inward from $3.3\,R_\odot$. This process is well understood and likely detected in young binaries (*30, 31*).

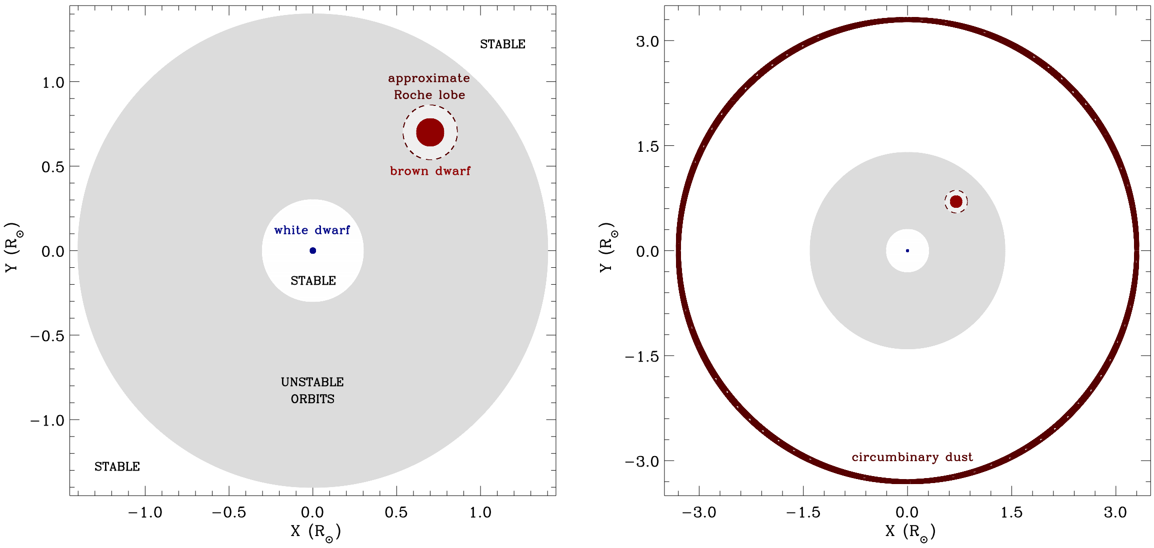

Figure 3: Circumbinary system geometry. Diagrams illustrating SDSS 1557 in the primary reference frame, where the entire system is drawn within a single plane as viewed from above, with the stable and unstable orbital regions (*24*) labelled on the left. The sizes of the binary components are accurately portrayed in both diagrams, and the companion is surrounded by a dashed boundary delineating a circular approximation of its Roche lobe.

The lifetime of an optically thin dust reservoir is determined by Poynting-Robertson (PR) drag, scaling linearly with particle size and yielding 9 yr for micron-sized grains orbiting SDSS 1557 at 3.3 $R_\odot$. Therefore, the circumbinary dust disk surrounding – and polluting – the white dwarf is either 1) in a transient phase of rapid erosion, 2) being replenished by additional dust sources, or 3) contains a significant mass of particles larger than 10-30 μm. In the second case, the observed 1100 K dust shell could be fed by an exterior, flat and cold disk that is beyond the gravitational influence of the binary.

Models of optically thin disk accretion onto single white dwarfs predict rates two orders of magnitude lower than that inferred to be ongoing in this system (*32*), where those calculations were made for vertically narrow (i.e. flat) disks, as expected from rapid dynamical relaxation around single stars. The accretion rate in this system therefore suggests the disk must have a significant vertical extent. As PR drag drives particles inward towards SDSS 1557, they will eventually experience gravitational encounters with the binary, and this could produce and maintain a vertically thick yet optically thin, disk configuration. Comparing the current, estimated rate of accretion with the theoretical maximum for PR drag on optically thin dust, implies the disk intercepts a fraction $\tau = 0.0025$ of the total starlight. However, this is only about half of $L_{\rm IR}/L_{*} = 0.0055$ obtained from fitting the spectral energy distribution, and may imply the accretion rate is actually more than twice the estimate based on models.

A cylindrical dust shell with radius $3.3\,R_{\odot}$ and height 1.1×10^{9} cm (1.0 white dwarf radius) would cover a fractional area of 0.0025. Such a shell might account for the observed ultraviolet fluxes shown in Figure 2, which sit below the atmospheric model and cannot be adequately explained by interstellar reddening, as this would result in a significantly lower effective temperature than derived here and by other authors (*3*). If correct, ultraviolet spectroscopy has the potential to detect gas absorption along the line of sight through the shell.

The progenitors of extant white dwarfs are typically A- and F-type stars with masses in the range $1.2 - 3.0\,M_{\odot}$, a stellar population that is not readily probed for inner planetary systems using conventional techniques. The SDSS 1557 binary was thus born with a low mass ratio in the range $M_2/M_1 = 0.02 - 0.05$, and likely with a semimajor axis less than an AU or so, in order to form a common envelope on the first ascent giant branch. Excepting the low mass ratio, the progenitor binary would have been similar to the eclipsing binaries with planets detected by *Kepler* (*33*). However, the surviving planetary bodies in the SDSS 1557 system likely had primordial orbits beyond a few AU to escape engulfment.

At the current steady-state accretion rate, over 10^{17} g of planetary debris has been deposited onto the white dwarf since its discovery in 2010. This is the bare minimum mass of the reservoir, yielding a parent body with diameter greater than 4 km for typical asteroid densities. This implies that the formation of large planetesimals in the SDSS 1557 system was not inhibited by the relatively massive substellar companion, and that destructive collisions among growing planetesimals were avoided.

If this polluted and dusty white dwarf is similar to the well-studied larger population, then the parent body of the debris was likely formed within the snow line of the progenitor system, and thus implying that rocky planet formation was robust in this circumbinary environment. These observations therefore support a picture where additional mechanisms can promote planetesimal growth in the terrestrial zones of close binary stars, which are predicted to be substantially wider than in planet forming disks around single stars (*34*). This interpretation can be confirmed with ultraviolet spectroscopy of key carbon and oxygen transitions, as these will easily distinguish between rocky and icy parent bodies.

References and Notes

1. Jura, M., Young, E. D. Extrasolar cosmochemistry, *Annu. Rev. Earth Planet. Sci.*, **42**, 45–67 (2014)

2. Farihi, J. Circumstellar debris and pollution at white dwarf stars, *New Astron. Rev.*, **71**, 9–34 (2016)

3. Girven, J., Gänsicke, B. T., Steeghs, D., Koester, D. DA white dwarfs in Sloan Digital Sky Survey Data Release 7 and a search for infrared excess emission, *Mon. Not. R. Astron. Soc.*, **417**, 1210–1235 (2011)

4. Farihi, J., Gänsicke, B. T., Steele, P. R., Girven, J., Burleigh, M. R., Breedt, E., Koester, D. A trio of metal-rich dust and gas discs found orbiting candidate white dwarfs with K-band excess, *Mon. Not. R. Astron. Soc.*, **421**, 1635 (2012)

5. Doyle, L. R., et al. Kepler-16: a transiting circumbinary planet, *Sci.*, **333**, 1602–1606 (2011)

6. Welsh, W. F., et al. Transiting circumbinary planets Kepler-34b and Kepler-35b, *Nat.*, **481**, 475–479 (2012)

7. Paardekooper, S., Leinhardt, Z. M., Thébault, P., Baruteau, C. How not to build Tatooine: the difficulty of in situ formation of circumbinary planets Kepler 16b, Kepler 34b, and Kepler 35b, *Astrophys. J.*, **754**, L16–L20 (2012)

8. Pelupessy, F. I., Portegies Zwart, S. The formation of planets in circumbinary discs, *Mon. Not. R. Astron. Soc.*, **429**, 895–902 (2013)

9. Lines, S., Leinhardt, Z. M., Paardekooper, S., Baruteau, C., Thebault, P. Forming circumbinary planets: N-body simulations of Kepler-34, *Astrophys. J.*, **782**, L11–L16 (2014)

10. Rafikov, R. R. Building Tatooine: suppression of the direct secular excitation in Kepler circumbinary planet formation, *Astrophys. J.*, **764**, L16–L21 (2013)

11. Martin, R. G., Armitage, P. J., Alexander, R. D. Formation of circumbinary planets in a dead zone, *Astrophys. J.*, **773**, 74–80 (2013)

12. Bromley, B. C., Kenyon, S. J., Planet formation around binary stars: Tatooine made easy, *Astrophys. J.*, **806**, 98–118 (2015)

13. Koester, D., Gänsicke, B. T., Farihi, J. The frequency of planetary debris around young white dwarfs, *Astron. Astrophys.*, **, 566**, A34–A53 (2014)

14. Vanderburg, A., et al. A disintegrating minor planet transiting a white dwarf, *Nat.*, **526**, 546–549 (2015)

15. Xu, S., Jura, M., Dufour, P., Zuckerman, B. Evidence for gas from a disintegrating extrasolar asteroid, *Astrophys. J.*, **816**, L22–L27 (2016)

16. Gänsicke, B. T., et al. High-speed photometry of the disintegrating planetesimals at WD 1145+017, *Astrophys. J.*, **818**, L7–L12 (2016)

17. Gänsicke, B. T., Koester, D., Farihi, J., Girven, J., Parsons, S. G., Breedt, E. The chemical diversity of exo-terrestrial planetary debris around white dwarfs, *Mon. Not. R. Astron. Soc.*, **424**, 333–347 (2012)

18. Farihi, J., Gänsicke, B. T., Koester, D. Evidence for water in the rocky debris of a disrupted extrasolar minor planet, *Sci.*, **342**, 218–220 (2013)

19. Fontaine, G., Brassard, P., Bergeron, P. The potential of white dwarf cosmochronology, *Publ. Astron. Soc. Pacific*, **113**, 409–435 (2001)

20. Sweigart, A. V. The determination of the core mass at the helium flash in globular cluster stars, *Astrophys. J.*, **426**, 612–620 (1994)

21. Marsh, T. R., Dhillon, V. S., Duck, S. R. Low-mass white dwarfs need friends ? five new double-degenerate close binary stars, *Mon. Not. R. Astron. Soc.*, **275**, 828–840 (1995)

22. Patten, B. M. et al. Spitzer IRAC photometry of M, L, and T dwarfs, *Astrophys. J.*, **651**, 502–516 (2006)

23. Casewell, S. L., et al. Multiwaveband photometry of the irradiated brown dwarf WD 0137–349B, *Mon. Not. R. Astron. Soc.*, **447**, 3218–3226 (2015)

24. Holman, M. J., Wiegert, P. A. Long-term stability of planets in binary systems, *Astrophys. J.*, **117**, 621–628 (1999)

25. Koester, D. Accretion and diffusion in white dwarfs, *Astron. Astrophys.*, **,** **498**, 517–525 (2009)

26. Debes, J. H. Measuring M dwarf winds with DAZ white dwarfs, *Astrophys. J.*, **652**, 636–642 (2006)

27. Maxted, P. F. L., Napiwotzki, R., Dobbie, P. D., Burleigh, M. R. Survival of a brown dwarf after engulfment by a red giant star, *Nat.*, **442**, 543–545 (2006)

28. Jura, M., Farihi, J., Zuckerman, B. Externally polluted white dwarfs with dust disks, *Astrophys. J.*, **663**, 1285–1290 (2007)

29. Farihi, J., Jura, M., Zuckerman, B. Infrared signatures of disrupted minor planets at white dwarfs, *Astrophys. J.*, **694**, 805–819 (2009)

30. Artymowicz, P., Lubow, S. H. Mass flow through gaps in circumbinary disks, *Astrophys. J.*, **467**, L77–L80 (1996)

31. Terquem, C., Sørensen-Clark, P. M., Bouvier, J. A circumbinary disc model for the variability of the eclipsing binary CoRoT 223992193, *Mon. Not. R. Astron. Soc.*, **454**, 3472–3479 (2015)

32. Bochkarev, K. V., Rafikov, R. R. Global modeling of radiatively driven accretion of metals from compact debris disks onto white dwarfs, *Astrophys. J.*, **741**, 36–44 (2011)

33. Kirk, B., et al. Kepler eclipsing binary stars. VII. the catalog of eclipsing binaries found in the entire Kepler data se, *Astron. J.*, **151**, 68–88 (2016)

34. Vartanyan, D., Garmilla, J. A., Rafikov, R. R. Tatooine nurseries: structure and evolution of circumbinary protoplanetary disks, *Astrophys. J.*, **816**, 94–112 (2016)

Acknowledgments The authors acknowledge Gemini Observatory for the award of Director's Discretionary Time for program GS-2012A-DD-3. The X-shooter observations were obtained under ESO programs 093.D-0030 and 097.C-0386. J. Farihi thanks R. Rafikov and D. Veras for useful discussions, and acknowledges support from the United Kingdom Science and Technology Facilities Council in the form of an Ernest Rutherford Fellowship (ST/J003344/1). S. G. Parsons and B. T. Gänsicke received financial support from the European Research Council under the European Union's 7th Framework Programmes n. 340040 (HiPERCAM) and n. 320964 (WDTracer), respectively.

Author contributions J. Farihi was the primary author, organized the observations, analyzed multi-wavelength data, implemented infrared models, and interpreted the overall data. S. G. Parsons reduced optical spectra, performed radial velocity and time-series analysis, and calculated all binary parameters. B. T. Gänsicke analyzed optical spectra and performed model atmosphere fitting to determine the primary stellar parameters. All authors contributed to and commented on the manuscript. Correspondence and requests for materials should be addressed to J. Farihi (j.farihi@ucl.ac.uk).

Methods

Observations and white dwarf parameters. The white dwarf SDSS 1557 was observed with three optical spectrographs covering the higher Balmer lines, and thus enabling as many independent determinations of $T_{\rm eff}$ and $\log\,g$. In addition to the ISIS spectrum previously published (*4*), new observations were obtained at Gemini South and the VLT. Director's Discretionary Time was awarded to obtain spectra covering important metal features as well as the higher Balmer lines using the GMOS spectrograph (*35*) on Gemini South in 2012 May, with the B600 grating and a $0.''75$ slit. Data were taken on two non-consecutive nights, with three individual exposures of 900 s obtained each night. Each of the six spectra were analyzed separately by fitting the temperature- and gravity-sensitive Balmer lines with white dwarf atmospheric models. This yields a statistical, weighted average of $T_{\rm eff} = 21\,800 \pm 600\,$K and $\log\,g = 7.50 \pm 0.10$, corresponding to $M = 0.40 \pm 0.04\,M_{\odot}$. The combined data are shown in Supplementary Figure 1 and reveal Ca II K absorption, whereas only Mg II was detected in the ISIS data. Analysis of individual GMOS spectra revealed $0.2 - 0.4\,$Å shifts in the Mg II line, but no firm conclusion could be reached due to the low spectral resolution and the small number of spectra.

Medium-resolution spectra covering the entire optical wavelength range were obtained with X-Shooter (*36*) on the VLT during two observing periods. In 2014 May, data were taken over two consecutive half nights, in below average weather conditions and without the benefit of the atmospheric dispersion corrector. The instrument was used in staring mode as the target is too faint to yield usable signal in the NIR arm of the spectrograph. A total of 18 usable spectra were acquired, each with roughly 1200 s exposure in both the UVB and VIS arms using the $0.''8$ and $0.''7$ slits respectively. With a similar instrument setup in 2016, SDSS 1557 was observed on 14 separate nights between Apr and Aug, yielding a total of 42 individual spectra. All spectra were fitted individually with atmospheric models, resulting in $T_{\rm eff} = 21\,810 \pm 790\,{\rm K}$ and $\log\,g = 7.63 \pm 0.11$, corresponding to $M = 0.45 \pm 0.04\,M_{\odot}$. As this data set contains the largest number of exposures, the highest resolution, and S/N $\approx$ 20 per spectrum, the derived X-shooter parameters were adopted for SDSS 1557. A summary of all spectroscopic observations are given in Supplementary Table 1.

Radial velocity analysis. Using the Mg II 4482 Å line in each of the individual X-Shooter spectra, the radial velocity of the white dwarf was measured for each of the 60 observations. Each spectrum was fitted with a combination of a straight line and a Gaussian around the absorption line, with the central position of the Gaussian allowed to vary, and the errors determined using the method of damped least-squares. The resulting velocity measurements and uncertainties are given in Supplementary Table 2, and were fitted with a sine wave of the form:

$$v(t) = \gamma_1 + K_1 \sin\left[\frac{2\pi(t - t_0)}{p}\right], \tag{1}$$

where p is the orbital period and t_0 is the time of inferior conjunction of the white dwarf. The results of this fit are detailed in Table 1 of the main paper, including the 2.273 hr binary period.

The only spectral features visible from the companion in the X-shooter data are emission lines arising from its heated inner hemisphere, with the Hα line strongest. The radial velocity of the Hα emission was measured using the same method as the white dwarf Mg II velocity measurements, but with one Gaussian for the white dwarf absorption component and another Gaussian for the emission feature. The latter was allowed to vary in position and strength, as the strength of irradiatively driven lines is phase dependent. The measured radial velocity semi-amplitude of the Hα emission line was $K_{\rm em} = 267.6 \pm 2.6\,{\rm km\,s^{-1}}$, where the radial velocities of the observed emission and the companion center-of-mass are related by (*38*):

$$K_2 = \frac{K_{\rm em}}{1 - [f(1+q)R_2/a]}, \tag{2}$$

where $q = M_2/M_1$ is the binary mass ratio, R_2 is the radius of the secondary, and a is the orbital separation. Here, f is a constant bound by the two extreme cases: all emission is from the substellar point and $f = 1$; the emission is spread uniformly over the surface, thus tracking the center-of-mass and $f = 0$. These extremes place limits on the actual radial velocity of the brown dwarf, yielding 0.056 $M_\odot$ (59 $M_{\rm Jup}$) $<$ M_2 $<$ 0.068 $M_\odot$ (71 $M_{\rm Jup}$), confirming a substellar nature. However, it is highly probable that the emission originates only from the heated hemisphere of the companion, and a more accurate estimate of the physical and binary parameters can be made by assuming the companion emission is uniformly spread across the inner hemisphere. This approach has been substantiated by observations of spectroscopic binaries where the secondary exhibits both heated emission and intrinsic absorption components (*38*). In this case $f = 0.42$ and the estimate of the true radial velocity is $K_2 = 288.3 \pm 3.0\,{\rm km\,s^{-1}}$, with a secondary mass of $0.063\,M_\odot$ (66 $M_{\rm Jup}$) as given in the main paper.

Modeling of companion, dust, and accretion. The infrared properties of SDSS 1557 were modeled in the context of previously published multi-wavelength photometry (*4*), including *Spitzer* IRAC data, but now as a binary system with well-constrained parameters. Previous modeling of the strong infrared excess detected in the $2-5\,\mu$m range employed only the standard, flat and opaque dust disk geometry, whose temperature-radius relationship is given by (*39*):

$$r \approx \left(\frac{2}{3\pi}\right)^{1/3} \left(\frac{T_{\rm eff}}{T}\right)^{4/3} R_* \tag{3}$$

where T is the dust temperature and R_* is the stellar radius. Based on the photometric spectral energy distribution shown in Figure 2, this model predicts a disk that extends from $0.4\,R_\odot$ and $T = 1400\,$K, to $0.8\,R_\odot$ and $T = 800\,$K (*4*). However, in light of the binary properties, there are no stable orbits within this entire region (*24*) and hence the canonical disk model can be ruled out.

Next the companion was modeled using published absolute magnitudes and infrared photometry for L-type dwarfs (*22, 40*). Four models for the companion were constructed by adopting typical absolute magnitudes for L0, L3, L5, and L8 dwarfs in the JHK and IRAC bands, then adjusting their flux to the 520 pc distance of the SDSS 1557 system. The best fit was found for an L5-type companion, as this is most consistent with the $1-2\,\mu$m photometry, but an L3 dwarf is just allowed within the errors. Spectral types later than L5 are also possible, as 100% of the observed infrared excess could be due to dust emission.

No cool dwarf emission can account for the strong excess at IRAC wavelengths, and a blackbody dust model was successfully fitted to the infrared photometry. This model has a temperature-radius dependence of (*41*):

$$r \approx \frac{1}{2} \left(\frac{T_{\rm eff}}{T}\right)^{2} R_* \tag{4}$$

For the $T = 1100\,$K dust model shown in Figure 2, blackbody grains have an orbital radius of 3.3 $R_\odot$ and lie in the stable circumbinary region.

Three models were tested to account for the ongoing accretion in SDSS 1557, as evidenced by the photopsheric metals detected in several data sets spanning over six years. The inferred rate of accretion is based on a steady-state balance that is highly likely given the diffusion timescale of only a few weeks (*25*), and based on the published magnesium abundance [Mg/H] $= -4.5$ (*4*). In a steady state, the total mass accretion rate onto the primary can be calculated as follows (*2*):

$$\dot{M}_1 \approx \frac{1}{A}\frac{X_{\mathrm{Mg}}\, M_{\mathrm{mix}}}{\tau_{\mathrm{Mg}}} \approx 6 \times 10^8\,\mathrm{g\,s^{-1}} \tag{5}$$

where M_{mix} is the stellar mass above Rosseland optical depth 2/3 where the accreted material is fully mixed, X_{Mg} is the mass fraction of Mg within this atmospheric layer, τ_{Mg} is the sinking timescale for Mg, and A represents the mass fraction of Mg within the source material. Only one accretion model can account both for the circumbinary dust and the atmospheric pollution in the star simultaneously, and that is direct deposition of material originating from the dust reservoir. Such a flow would be driven by Poynting-Robertson drag at a rate near $6.0 \times 10^8\,\mathrm{g\,s^{-1}}$ for a bulk Earth abundance of Mg [$A = 0.16$ (*45*)], which compares well with predictions based on the fractional infrared luminosity of the dust disk (*32*).

For completeness, two additional models assume that Mg is carried in solar abundance [$A = 0.00069$ (*47*)], via binary mass transfer as Roche lobe overflow or in a captured, wind-like outflow from the substellar companion. In these cases the total mass accretion rate would be at least $1.4 \times 10^{11}\,\mathrm{g\,s^{-1}}$ ($2.3 \times 10^{-15}\,M_{\odot}\,\mathrm{yr^{-1}}$). For this system, the Roche lobe of the companion is well approximated by a circular radius (*37*):

$$\frac{R_L}{a} = 0.462\left(\frac{q}{1+q}\right)^{1/3} \tag{6}$$

This gives $R_L = 0.16\,R_{\odot}$ and is twice as large as models predict for substellar objects of $0.063\,M_{\odot}$ at ages of a few to several Gyr (*42*). There are some analogies between this system and hot Jupiter exoplanets, where inflated radii have been directly observed (*43*), and the incident flux received by the companion of SDSS 1557 is comparable at 7×10^9 erg s^{-1} cm^{-2}. However, hot Jupiters can be 100 times less massive than the brown dwarf in this system, and hence the energy requirement to inflate such an object would be commensurately greater. The system NN Ser has a 57 000 K white dwarf irradiating a $0.1\,M_\odot$ M dwarf with incident flux 3×10^{11} erg s^{-1} cm^{-2}, but precise measurements of the secondary radius reveal it to be only 10% larger than model predictions (*44*). It is therefore unlikely that the companion to SDSS 1557 is filling its Roche lobe.

If the white dwarf were instead accreting wind from the substellar companion, it would be an unexpected find; all known or suspected wind-accreting white dwarfs are in polars or detached binaries with stellar (M-type) companions (*38*). In the case that such material is optimally captured in a Bondi-Hoyle flow onto SDSS 1557, the required mass-loss from the companion can be expressed as (*26*):

$$\dot{M}_2 = \dot{M}_1 \left(\frac{a^2 v^4}{G^2 M_1^2} \right) \tag{7}$$

Here, v is taken as the wind velocity with orbital velocity ignored; this would only serve to increase $\dot{M}_2$. For an escape velocity of 600 km s^{-1} the required mass-loss rate from the companion is $1.5 \times 10^{-14}\,M_\odot$ yr^{-1} and nearly equal to the solar value. However, a more realistic, gravitational capture would be described as (*46*):

$$\dot{M}_2 = \dot{M}_1 \left(\frac{a^2 v^2}{G M_1 R_1} \right) \tag{8}$$

For the same parameters as above, this results in a companion wind rate of $4.3 \times 10^{-13}\,M_\odot\,\mathrm{yr}^{-1}$. Either case would require the brown dwarf to have a wind comparable to or higher than that of the Sun, and can hence be dismissed.

Therefore the best model for the ongoing accretion is due to radiatively driven infall from the circumbinary dust disk.

Data availability The spectroscopic data analyzed for radial velocity variations are available via the ESO and Gemini archives, while photometric data are previously published.

References

35. Hook, I., Jørgensen, I., Allington-Smith, J. R., Davies, R. L., Metcalfe, N., Murowinski, R. G., Crampton, D. The Gemini-North Multi-Object Spectrograph: performance in imaging, long-slit, and multi-object spectroscopic modes, *Publ. Astron. Soc. Pacific*, **116**, 425–440 (2004)

36. Vernet, J., et al. X-shooter, the new wide band intermediate resolution spectrograph at the ESO Very Large Telescope, *Astron. Astrophys.*, **536**, A105–A119 (2011)

37. Eggleton, P. P. Approximations to the radii of Roche lobes, *Astrophys. J.*, **268**, 368–369 (1983)

38. Parsons, S. G., et al. A precision study of two eclipsing white dwarf plus M dwarf binaries, *Mon. Not. R. Astron. Soc.*, **420**, 3281–3297 (2012)

39. Jura, M. A tidally disrupted asteroid around the white dwarf G29-38, *Astrophys. J.*, **584**, L91–L94 (2003)

40. Dahn, C. C., et al. Astrometry and photometry for cool dwarfs and brown dwarfs, *Astron. J.*, **124**, 1170–1189 (2002)

41. Wyatt, M. C. Evolution of debris disks, *Annu Rev. Astron. Astrophys.*, **46**, 339–383 (2008)

42. Baraffe, I., Chabrier, G., Barman, T. S., Allard, F., Hauschildt, P. H. Evolutionary models for cool brown dwarfs and extrasolar giant planets, *Astron. Astrophys.*, **402**, 701–712 (2003)

43. Fortney, J. J., et al. Discovery and atmospheric characterization of giant planet Kepler-12b: an inflated radius outlier, *Astrophys. J. Supp.*, **197**, 9–20 (2011)

44. Parsons, S. G., Marsh, T. R., Copperwheat, C. M., Dhillon, V. S., Littlefair, S. P., Gänsicke, B. T., Hickman, R. Precise mass and radius values for the white dwarf and low mass M dwarf in the pre-cataclysmic binary NN Serpentis, *Mon. Not. R. Astron. Soc.*, **402**, 2591–2608 (2010)

45. Allègre, C., Manhès, G., Lewin, É. Chemical composition of the Earth and the volatility control on planetary genetics, *Earth Planet. Sci. Let.*, **185**, 49–69 (2001)

46. Farihi, J., Barstow, M. A., Redfield, S., Dufour, P., Hambly, N. C. Rocky planetesimals as the origin of metals in DZ stars, *Mon. Not. R. Astron. Soc.*, **404**, 2123–2135 (2010)

47. Lodders, K. Solar system abundances and condensation temperatures of the elements, *Astrophys. J.*, **591**, 1220–1247 (2003)

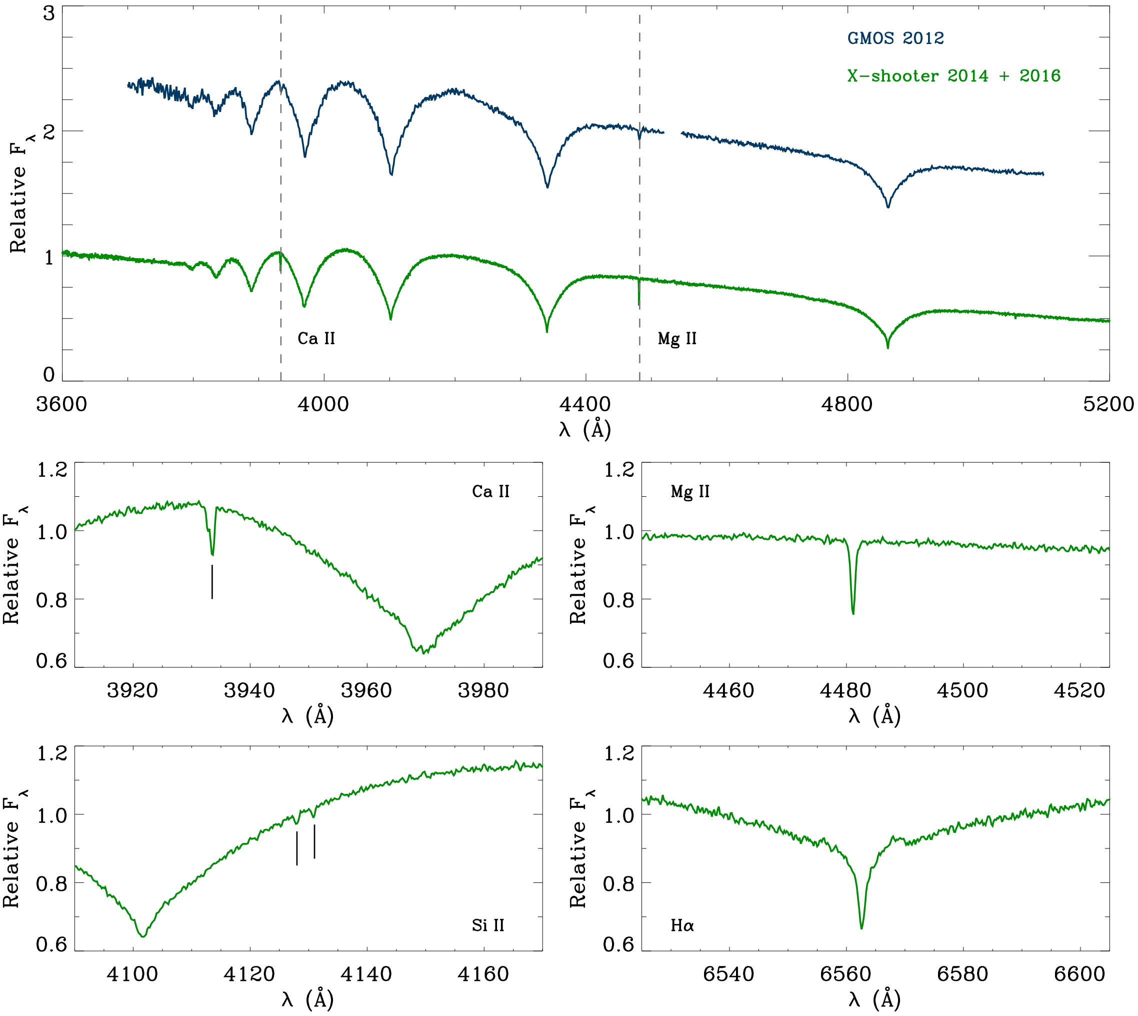

Supplementary Figure 1: Spectroscopic data plots. The top panel shows the combined GMOS data set in blue. In addition to the Mg II 4482Å feature detected previously in the ISIS spectrum, the Ca II K line is also clearly detected; this is unprecedented at low-resolution for a $T_{\rm eff} > 20\,000$K, hydrogen atmosphere white dwarf. In green is the velocity-shifted and combined, X-Shooter spectrum over the same wavelength range. The lower four figures focus on individual line regions within the X-shooter data, where notable features include emission components in both Hα and Ca II K. Because these data are co-added in the rest frame of the white dwarf, the weak Hα emission from the irradiated companion is smeared over a wide velocity range, resulting in the small amount of structure flanking the sharp photospheric absorption. Weak lines of Si II are visible as shown at 4128, 4131 Å, and also (not shown) at 5056, 6347 Å.

Epoch	2010.4	2012.4	2014.4, 2016.3–2016.6
Facility	WHT	Gemini South	VLT
Spectrograph	ISIS	GMOS	X-shooter
$\lambda/\Delta\lambda$	2300	1600	6000
λ (Å)	3650–5120	3610–6450	3000–10 2000
# Spectra	3	6	60
Detected Metals	Mg II	Mg II, Ca II	Mg II, Si II, Ca II
$T_{\rm eff}$ (K)	$22\,250 \pm 1190$	$21\,800 \pm 600$	$21\,810 \pm 790$
log g (cm s^{-2})	7.61 ± 0.36	7.50 ± 0.10	7.63 ± 0.11
M ($M_\odot$)	0.43 ± 0.14	0.40 ± 0.04	0.45 ± 0.04

Supplementary Table 1: Summary of spectroscopic observations. In addition to the spectrum available from the SDSS,there were three follow up, spectroscopic data sets obtained for SDSS 1557, whose details are listed in the table. Within each data set, the higher Balmer lines for individual spectra were fitted with atmospheric models to obtain $T_{\rm eff}$ and $\log g$, where the listed values and errors in the table are the resulting means and standard deviations, respectively. Stellar masses are derived from evolutionary models, with errors propagated from the uncertainties in $T_{\rm eff}$ and $\log g$. The approximate resolving power $R = \lambda/\Delta\lambda$ is given at 4000 Å. The X-shooter values were adopted for this work, as these data are of the highest quality and spectral resolution.

HJD	Radial Velocity ($\mathrm{km\,s^{-1}}$)	Error ($\mathrm{km\,s^{-1}}$)	HJD	Radial Velocity ($\mathrm{km\,s^{-1}}$)	Error ($\mathrm{km\,s^{-1}}$)
56 798.602714	43.85	5.62	57 488.821731	−16.57	3.27
56 798.620193	−8.53	4.58	57 488.830599	−10.38	3.54
56 798.637932	−25.42	4.92	57 488.839467	9.88	4.54
56 798.655365	3.76	4.54	57 512.721651	36.55	3.31
56 798.672982	52.03	4.29	57 512.730518	58.61	3.37
56 798.690741	45.63	4.77	57 512.739384	63.01	3.21
56 798.708633	6.45	4.90	57 512.748670	52.09	3.19
56 798.739539	−18.84	4.71	57 512.757559	29.85	3.25
56 798.757188	24.90	4.73	57 512.766426	9.63	3.17
56 798.769488	41.84	11.32	57 512.775554	−5.40	3.02
56 799.679388	−17.17	5.31	57 512.784445	−9.75	3.21
56 799.695131	−0.67	4.96	57 512.793335	−7.41	3.20
56 799.713580	40.20	5.87	57 566.532498	56.37	3.55
56 799.729323	54.91	8.13	57 566.541386	55.72	3.56
56 799.747266	14.84	14.33	57 566.550262	36.20	3.34
56 799.763003	−29.29	14.22	57 569.571379	61.02	2.89
56 799.781362	−18.10	11.44	57 569.580259	55.07	2.99
56 799.797089	23.01	20.21	57 569.589125	21.26	3.02
57 486.793931	58.20	3.12	57 569.609550	−20.62	3.06
57 486.802812	39.27	3.39	57 569.618431	−22.69	2.97
57 486.811696	15.03	3.46	57 569.627298	3.82	3.02
57 486.823164	−15.73	3.42	57 597.534207	2.43	3.79
57 486.832047	−26.81	3.55	57 597.543096	−8.28	3.51
57 486.840931	−14.69	3.32	57 597.551991	−21.79	3.97
57 486.852416	10.89	3.22	57 601.534731	−19.29	3.03
57 486.861294	32.82	3.35	57 601.543618	−9.66	3.23
57 486.870173	54.40	3.40	57 601.552518	11.86	3.61
57 488.783416	65.05	3.48	57 603.486847	39.71	3.89
57 488.792296	42.14	3.90	57 603.495741	21.08	5.72
57 488.801179	17.24	4.05	57 603.504640	7.37	4.11

Supplementary Table 2: Mg II 4482Å velocity measurements from the X-shooter data. The velocities were determined by fitting each absorption profile with a combination of a Gaussian and a straight line, with the error derived using the damped least-squares method.